Physics of the Earth and Planetary Interiors 265 (2017) 1–14

Contents lists available at ScienceDirect

Physics of the Earth and Planetary Interiors

journal homepage: www.elsevier.com/locate/pepi

Crustal structure of northern Italy from the ellipticity of Rayleigh waves

Andrea Berbellini [a,b,*], Andrea Morelli [b,a], Ana M. G. Ferreira [c,d]

[a] Dipartimento di Fisica e Astronomia, Alma Mater Studiorum – Università degli Studi di Bologna, Via Zamboni 33, 40126 Bologna, Italy
[b] Istituto Nazionale di Geofisica e Vulcanologia, Sezione di Bologna, Via Donato Creti 12, 40128 Bologna, Italy
[c] Department of Earth Sciences, Faculty of Maths & Physical Sciences, University College London, WC1E6BT, United Kingdom
[d] CERIS, Instituto Superior Tecnico, Universidade de Lisboa, Av. Rovisco Pais 1, 1049-001 Lisboa, Portugal

ARTICLE INFO

Article history:
Received 26 October 2016
Received in revised form 19 December 2016
Accepted 20 December 2016
Available online 3 February 2017

ABSTRACT

Northern Italy is a diverse geological region, including the wide and thick Po Plain sedimentary basin, which is bounded by the Alps and the Apennines. The seismically slow shallow structure of the Po Plain is difficult to retrieve with classical seismic measurements such as surface wave dispersion, yet the detailed structure of the region greatly affects seismic wave propagation and hence seismic ground shaking.

Here we invert Rayleigh wave ellipticity measurements in the period range 10–60 s for 95 stations in northern Italy using a fully non linear approach to constrain vertical v_S, v_P and density profiles of the crust beneath each station. The ellipticity of Rayleigh wave ground motion is primarily sensitive to shear-wave velocity beneath the recording station, which reduces along-path contamination effects. We use the 3D layering structure in MAMBo, a previous model based on a compilation of geological and geophysical information for the Po Plain and surrounding regions of northern Italy, and employ ellipticity data to constrain v_S, v_P and density within its layers. We show that ellipticity data from ballistic teleseismic wave trains alone constrain the crustal structure well. This leads to MAMBo-E, an updated seismic model of the region's crust that inherits information available from previous seismic prospection and geological studies, while fitting new seismic data well. MAMBo-E brings new insights into lateral heterogeneity in the region's subsurface. Compared to MAMBo, it shows overall faster seismic anomalies in the region's Quaternary, Pliocene and Oligo-Miocene layers and better delineates the seismic structures of the Po Plain at depth. Two low velocity regions are mapped in the Mesozoic layer in the western and eastern parts of the Plain, which seem to correspond to the Monferrato sedimentary basin and to the Ferrara-Romagna thrust system, respectively.

© 2017 The Authors. Published by Elsevier B.V. This is an open access article under the CC BY license (http://creativecommons.org/licenses/by/4.0/).

1. Introduction and geological context

The Po Plain is the largest sedimentary basin in Italy. It extends in a west-east direction from the western Alps to the Adriatic sea and it is bounded by the Apennines chain to the South with a total surface of ≈ 48,000 km^2. It is one of the most densely populated areas in Italy, with a population of ≈ 20 millions, and one of the most important industrial districts. At the surface, the Po Plain looks like a large, flat and uniform plain, which is a relatively rare shape in the generally tectonically-active Italian context. Over the past centuries, this feature enhanced the concentration of human activities in this area because of the fertility of the land and the easier connections between the cities.

From a geological point of view, this sedimentary basin corresponds to the ancient African foreland environment, now being squeezed between the Alps and the Apennines. It is filled by a superposition of Pliocene-Quaternary deposits with thickness ranging between a few hundred meters (above the buried thrust systems) to 8 km (above the depocenters). Sedimentary layers cover completely a complex system of buried faults that run roughly parallel to the Apennines chain in the southern-middle part of the plain. The Po Plain is divided into three main structural segments, the Ferrara-Romagna Arc, the Emilia Arc and the Monferrato Arc from the East to the West, respectively (Fig. 1). A buried thrust system lies in the north, parallel to the Alpine chain, from western Alps to the Garda Lake region where it connects to the Giudicarie thrust system (GS, Fig. 1, Vannoli et al., 2015).

The building of the Alps and Apennines — although with quite different characteristics — is linked to the convergence of the European and African plates. This process is still ongoing today, with a

* Corresponding author at: Department of Earth Sciences, Faculty of Maths & Physical Sciences, University College London, WC1E6BT, United Kingdom.
E-mail address: a.berbellini@ucl.ac.uk (A. Berbellini).

http://dx.doi.org/10.1016/j.pepi.2016.12.005
0031-9201/© 2017 The Authors. Published by Elsevier B.V.
This is an open access article under the CC BY license (http://creativecommons.org/licenses/by/4.0/).

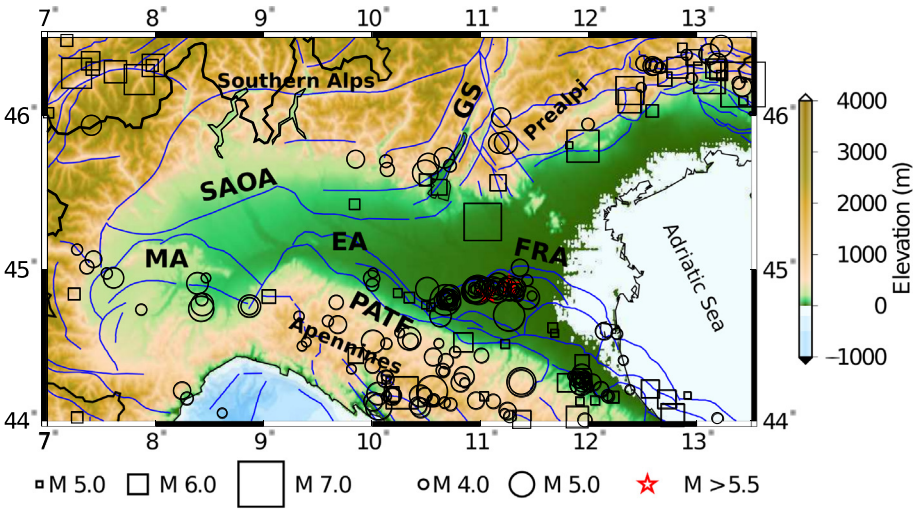

Fig. 1. Main structural elements of the Po Plain (Barrier et al., 2005) FRA: Ferrara-Romagna Arc; EA: Emilia Arc; MA: Monferrato Arc; PATF: Pedeapeninnic thrust front; SAOA: Southern Alps Outer Arc; GS: Giudicarie System. Squares: Historical seismicity before 1985 ($M > 5.0$) from the CPTI11 catalogue (http://emidius.mi.ingv.it/CPTI11/) and ISIDE catalogue (http://iside.rm.ingv.it). Circles: Instrumental seismicity from 1985 to present day ($M > 4.0$). Stars: Instrumental earthquakes with magnitude $M > 5.5$. The blue lines correspond to faults (Barrier et al., 2005).

convergence rate of 3–8 mm/year (Serpelloni et al., 2007). The Adria promontory (bounded by the easternmost Apennines, and including the Adriatic Sea) is rotating counter-clockwise with a rotational pole located in the western Alps. For this reason the convergence rate in eastern Po Plain is higher than in the western part. The tectonic activity generates a relatively moderate seismicity (compared to other Italian zones) but still significant enough to cause occasional, but notable, damage to human activities. The last important seismic sequence hit the Ferrara region in May and June 2012, originating on the Ferrara-Romagna Arc. The two mainshocks struck on 2012 May 20 (M_w 6.1) and 2012 May 29 (M_w 5.9). These events caused a total of $\approx$ 500 injuries, 27 deaths and $\approx$ 20,000 evacuations. They also caused heavy damage to historical buildings and an overall damage to the residential and productive infrastructure with value estimated in the order of billions of Euros. Emilia-Romagna's regional government gave a partial estimate of damages of 2.7 billions of Euros, for the industrial sector only (www.regione.emilia-romagna.it/terremoto/nove-mesi-dal-sisma/). The effects of the earthquakes were much larger than expected as the ground-shaking recorded exceeded the EC8[1] recommendation of the European Union (Dujardin et al., 2016). This was due to the basin effect of the sedimentary structure with slow and thick layers over a crystalline and fast basement structure.

Sedimentary basins have a strong effect on the amplitude of ground-shaking and on seismic wave propagation. These effects have been observed and studied in many instances, from the 1985 Mexico City earthquake (Bard et al., 1998) to the recent 2010 Darfield (New Zealand) earthquake (Bradley, 2012). Other studies on this topic have been performed by Aagaard et al. (2008) on the Los Angeles basin, Koketsu and Kikuchi (2000) and Dhakal and Yamanaka (2013) on the Kanto basin (Japan) and by Stupazzini et al. (2009) and Chaljub et al. (2010) on the Grenoble basin. All of these studies showed that sedimentary structures strongly amplify the amplitudes of surface waves. The knowledge of the shallow structure in sedimentary terrains — such as the Po Plain — has then a crucial importance for hazard calculation and ground-shaking assessment.

[1] EN 1998-1 (2004): Eurocode 8: Design of structures for earthquake resistance — Part 1: General rules, seismic actions and rules for buildings [Authority: The European Union Per Regulation 305/2011, Directive 98/34/EC, Directive 2004/18/EC].

Crustal seismological models currently available for northern Italy have been mostly developed at a regional scale. EPcrust (Molinari and Morelli, 2011) is a continental crustal model of the European plate, from northern Africa to the North Pole, with a resolution of $0.5^\circ \times 0.5^\circ$. This model has been built by collecting and integrating previous seismological studies in the region. It is parameterised using a 3-layer setting: sedimentary, upper crust and lower crust. It is not useful for local-scale modelling because of its low resolution. Diehl et al. (2009) focused their attention on the western part of the Alpine region, building a 3-D crustal model by a classical technique based on first arriving P-phases picked on a good-quality teleseismic dataset. Wagner et al. (2012) built a 3-D model of the Alps by the combination of two tomographic techniques: controlled-source seismology (CSS) and local earthquake tomography (LET). Gualtieri et al. (2014) built a model of the crust and shallow mantle of the Italian region and a revised map of the Moho depth using regional travel time tomography. The model has a lateral resolution of 0.1 degrees and 2 km vertical resolution. Molinari et al. (2015b) obtained a 3-D model of Italy and the Alpine region by using phase and group velocities from ambient noise cross-correlation (Verbeke et al., 2012). They used the same parameterisation scheme as EPcrust, with a resolution of $0.25^\circ \times 0.25^\circ$.

None of these models has enough resolution for local-scale seismic waveform studies, as needed for hazard assessment and calculation of earthquake scenarios. The more recent model MAMBo (Molinari et al., 2015a) represents the 3D crustal structure in the Po Plain area with better detail. It has been built with the purpose of improving the ability of simulating and predicting the effects of earthquakes in the Po Plain. The shallow seismic structure (v_P, v_S, density) of the sedimentary filling has been defined by merging all available geological and geophysical information, mostly extracted from the abundant prospection work that has been performed in the last decades for hydrocarbon exploration. The model has resolution of $0.01^\circ \times 0.01^\circ$, with a very detailed description of the interfaces between the sedimentary layers (Fig. 2). Velocities inside each layer are defined following empirical relations resulting from laboratory studies (Brocher, 2005), using profiles made by two gradients in each layer (Fig. 2). Each stratigraphic layer varies laterally in thickness, but there is no lateral variation of its seismic parameters. Molinari et al. (2015a) showed that MAMBo

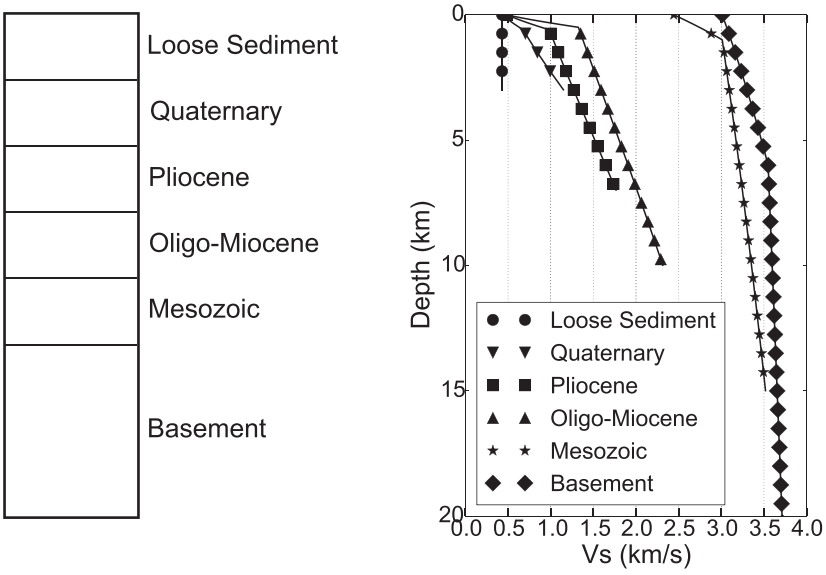

Fig. 2. Left: stratigraphic column of the Po Plain. Right: Gradients of v_S relative to each stratigraphic layer used in the construction of the MAMBo model (redrawn after Molinari et al., 2015b).

is able to predict the amplitude and duration of seismograms originating from an earthquake in the Plain better than previously available models. Nevertheless, the use of empirical relations to estimate the physical properties of the subsurface is a limitation of MAMBo. Thus, an improvement of the MAMBo model using information from actual seismic recordings rather than from compilations of information is a key priority to better simulate seismic propagation, ground-shaking and local effects in the Po Plain.

MAMBo covers a very shallow section of the crust, down to $\approx$ 10 km depth. This is indeed the most significant domain for modelling seismic wave propagation in hazard studies. Such a shallow depth cannot be properly imaged using earthquake-based tomographic techniques — such as surface-wave phase/group velocity, or body-wave travel times — because of scarcity of local seismicity. Regional-distance paths do not reach optimal sensitivity at such shallow depth. We thus use a seldomly used seismic observable: the aspect ratio of elliptically-polarised Rayleigh wave ground motion from teleseismic events. Ellipticity of Rayleigh waves, also called H/V ratio, is defined as the ratio between the amplitude of the horizontal component of Rayleigh wave motion over its vertical component. It does not depend on the source or the path of the wave, but it depends only on the structure beneath the receiving station (e.g., Ferreira and Woodhouse, 2007a,b). It is mostly sensitive to shallow values of shear-wave velocity (Fig. 3) but the sensitivity to v_P and density is not negligible either. In Fig. 3 we can also notice that ellipticity kernels change sign at any fixed period at rather shallow depth, where amplitude is large. As a consequence, either a shallow lower velocity, or an appropriately deeper higher velocity, can increase H/V. The zero crossing shifts deeper as the wave period considered increases, making a broad band inversion much less sensitive to this uncertainty. Also, since we perform a fully linear Monte Carlo inversion, we do not actually use linearised sensitivity kernels in our work, but it is instructive to examine them to understand what part of the structure influences our observables.

H/V ratios have been used in the last decades mostly for soil characterisation and micro-zonation and they have been measured mostly on seismic noise by spectral ratio analysis (Nakamura, 1989). Such measurements on ambient noise can be performed at very short periods, being sensitive to the top few hundred metres of the subsurface, which is not the scope of this study.

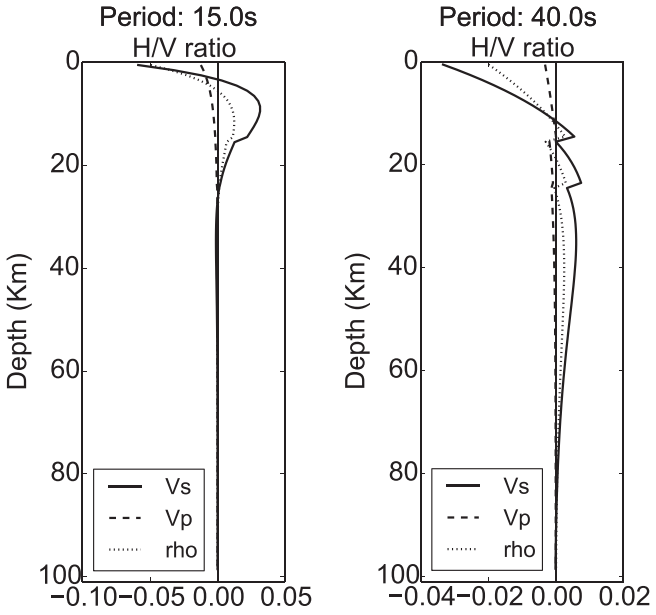

Fig. 3. Sensitivity kernels of H/V ratio at wave periods T = 15 s and T = 40 s to v_S (solid line), v_P (dashed line) and density (dotted line) calculated by finite differences using a normal mode formalism for the 1-D PREM Earth model (Dziewonski and Anderson, 1981).

We use instead measurements of ellipticity based on seismic signals from teleseisms, with a longer period range and thus with sensitivity spread over the whole crustal depth. A few studies have carried out similar measurements in different regions (e.g., Ferreira and Woodhouse, 2007a; Tanimoto and Rivera, 2008; Lin et al., 2012) but the full scope of teleseismic ellipticity measurements and inversion has not been fully explored yet.

The aim of this work is to build a new model of the crust of northern Italy using ellipticity measurements based on teleseismic recordings. We use a wide dataset of ellipticity curves measured previously by Berbellini et al. (2016) at 95 seismic stations in northern Italy from $\approx$ 500 teleseisms from all over the world in the period range 10s-110s. Since Rayleigh-wave ellipticity is non-linearly related to shear-wave structure, we implement a fully

non-linear Monte Carlo inversion method based on the Neighbourhood sampling algorithm (Sambridge, 1999) and we perform a full inversion of all the data available. We keep the layered structure of MAMBo unchanged and we invert for shear wave speed inside each layer. We then interpolate by ordinary kriging the values obtained for each layer and for each station and we build a new crustal model, with the same layered structure as MAMBo, but with laterally changing values of shear-wave velocity. Therefore the new model merges information from different approaches: geological and geophysical field studies (through the interfaces structure of MAMBo) and seismological modelling (from ellipticity inversions). Our goal is to build a model with high lateral resolution, layering based on the main geological discontinuities, and reliable details in the shallowest layers — where usually tomographic models do not have their best resolution. In the following, we will briefly recall the dataset used — obtained in Berbellini et al. (2016) — followed by an explanation of the inversion technique, including some synthetic recovery tests. We then describe and discuss the resulting model.

2. Dataset

We use a large dataset of ellipticity curves measured by Berbellini et al. (2016) for 95 broadband seismic stations in northern Italy in the period range 10–110 s. Ellipticity curves have been obtained by measuring H/V ratios on seismic signals of approximately 500 teleseisms from all over the world. For each earthquake the Rayleigh wave fundamental mode has been extracted from the rest of the record by analysing the phase shift between vertical and radial component Rayleigh waves, and time-windowing the signal where the phase shift is 90°, as expected for the Rayleigh wave fundamental mode. Ellipticity has then been calculated as the average ratio between the envelopes of vertical and radial component amplitude data. Finally, median and percentiles have been used to define a single representative ellipticity curve and uncertainties for each station. For more details about the measurement technique, we refer the reader to the study of Berbellini et al. (2016). The distribution of the measurements used to build the ellipticity curves is shown in Fig. 4 and the number of measurements as a function of wave period are given in Table. 1. As reported by Berbellini et al. (2016), measured ellipticity curves show higher H/V values for stations located on the Plain (Figs. 5) compared to stations on the mountains. This effect is particularly evident at short wave periods. This is due to the very slow shear-velocity waves at shallow depth in the Plain associated with the high sensitivity of ellipticity to the shallowest layers of the crust (Fig. 3).

Fig. 5 compares measured H/V values at T = 11 s and T = 16 s with theoretical values calculated using a normal mode formalism (Herrmann et al., 2013) for the MAMBo model (Molinari et al., 2015a). The comparison shows a larger mismatch for the stations in the Plain than for the stations on the mountains. This shows that there is room for improvement in MAMBo to better match the seismological observations.

3. Inversion technique

Yano et al. (2009) and Tanimoto et al. (2013) inverted ellipticity curves using a linearised method. Yano et al. (2009) noticed a strong dependence of the final solution on the starting model — not surprising, given known difficulties of linearised methods to tackle strong non-linearity, as present in this case — and showed that ellipticity is able to improve resolution of shallow structure in a joint inversion with other seismic observables, such as phase and group velocities. We will instead invert ellipticity data alone

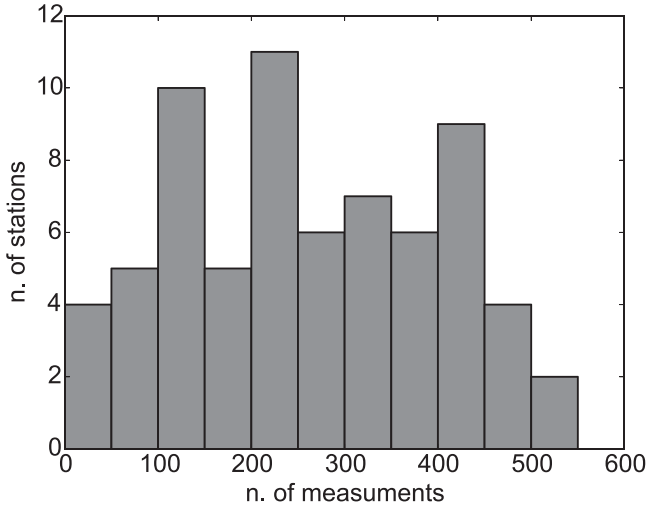

Fig. 4. Histogram of the number of measurements performed for each station.

— although subject to constraints, as will be shown — and in this endeavour, to avoid local minima, we resort to a fully non linear Monte Carlo inversion.

We chose the neighbourhood sampling algorithm, as described and implemented by Sambridge (1999). This method samples the model space in a very efficient way in order to find an ensemble of models that minimise a cost function, which describes the ability of a model to fit observed data, together with its likelihood according to some a priori knowledge. As explained in detail below, we define our cost function by summing a term describing the misfit between observed and theoretical ellipticity data, and a term describing the difference from an a priori model.

For each model sampled we calculate the theoretical ellipticity curve using a normal mode approach (Herrmann, 2013). Theoretical ellipticity is calculated as the ratio between the horizontal and the vertical eigenfunctions evaluated at the Earth's surface of the spheroidal mode equivalent to the Rayleigh wave considered (Ferreira and Woodhouse, 2007b). Observed ellipticity is taken from the measurements by Berbellini et al. (2016). We assume that measurements $i = 1, \ldots N$ have uncorrelated Gaussian variances ${\sigma_D^i}^2$, and that the a priori model also has uncorrelated uncertainties ${\sigma_M^i}^2$ on model parameters $j = 1, \ldots P$. We find the solutions that minimise the cost function:

$$c = ||g(m) - d||^2_{C_D^{-1}} + ||m - m_{prior}||^2_{C_M^{-1}}, \quad (1)$$

where the diagonal matrices C_D^{-1} and C_M^{-1} are formed by the uncertainties ${\sigma_D^i}^2$ and ${\sigma_M^i}^2$ respectively. Eq. (1) that can be re-written as:

$$c = \sum_{i=1}^{N} \frac{\left(g^i(m) - d^i_{obs}\right)^2}{{\sigma_D^i}^2} + \sum_{j}^{P} \frac{\left(m^j - m^j_{prior}\right)^2}{{\sigma_M^j}^2}$$

where d^i_{obs} are the observed data, $g^i(m)$ are the theoretical values calculated for a given trial model m, σ^i_D is the variance of the measurement calculated on observed data and σ^i_M is the variance of the a priori model. We choose as σ_M the value corresponding to 50% of the a priori model. The first term in (1) represents the misfit between observed data and theoretical prediction for the specific candidate model sampled, whereas the second term defines the distance of the candidate model from the a priori model. The inversion procedure samples the model space seeking to minimise the misfit to the observed data without picking models too far from a reference model. This is important to avoid unrealistic models that may fit the data better. Since we do not impose any boundary to

Table 1
Average number of final measurements performed for each station and for each wave period; Average number of measurement per station: 270; Average number of teleseismic records available per station: 490.

Wave period	11 s	13 s	16 s	20 s	25 s	31 s	38 s	47 s	58 s
Average n. of measurements	146	204	248	253	248	223	194	164	136

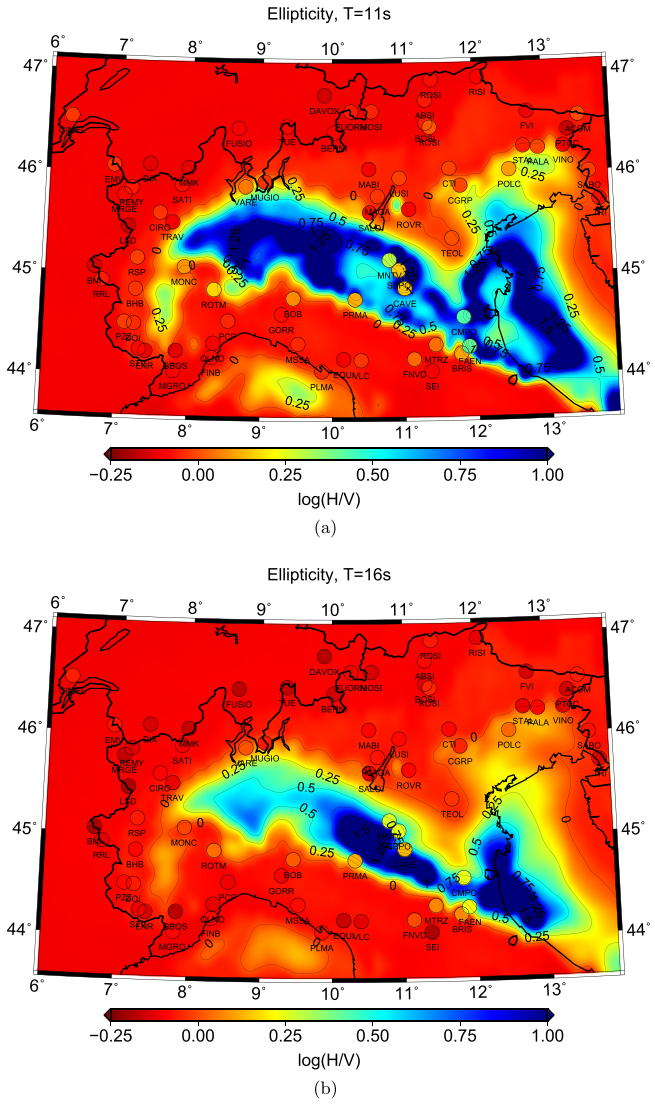

Fig. 5. Observed ellipticity (circles) compared to theoretical predictions for MAMBo (background) at period T = 11 s (a), and T = 16 s (b).

the distance from the reference model MAMBo, in principle a model can be very different from the reference one, but the new model must reproduce the observed data very well, otherwise it will gain a low cost function value and it will be rejected.

Also, for example if a layer is too thin and the data do not have enough sensitivity to resolve it, the system will choose a model close to the reference model and thus will avoid unrealistic features.

The geographically localised sensitivity of Rayleigh H/V ratio may discourage from inverting these data alone. In fact, the result of inversion is a profile below each station, and — particularly when stations are spaced at a scale larger than the expected structural variations, as in our case — one is left with the problem of interpolating among vertical profiles at different locations. Specific techniques, such as kriging (e.g., Davis, 2002), may help, but a likely consequence may be an unduly smooth model. We follow a different approach, and choose to use ellipticity data to tune the existing model MAMBo, by enabling lateral variations in shear-wave speed within its constituent domains. As explained in Section 1, model MAMBo describes in detail the geometry of shallow subsurface structure beneath the Plain. However, the seismic properties of the sedimentary layers (e.g., v_S) are not obtained from direct observations, but from laboratory and empirical relations related to geological information. New constraints on the crustal structure beneath the Po Plain, and neighbouring areas, can be obtained from ellipticity data given their strong sensitivity to shallow crustal structure. In our inversion, we honour the geometry of discontinuities among geological layers, and within these shapes we adjust the model parameters used to describe wave speed (baseline and slope with depth for each structural element). As we will see in the next section, the ellipticity data cannot precisely locate discontinuities, so we deem a better choice to fix them — including the Moho — to reliable values, as defined in MAMBo. We thus apply the non linear inversion scheme to the ellipticity curves for 95 stations available in the study region (Berbellini et al., 2016), using local MAMBo discontinuity depths as constraints. In our search, we let v_S vary, and scale v_P and density using the relations by Brocher (2005). In the following, when illustrating and discussing results of the inversion we will only refer to v_S, but variations proportionally affect P-wave velocity and density as well — as we find that an inversion for only v_S would have limited significance investigating. Whether widely-adopted Brocher (2005) scaling relations are always appropriate for our region is beyond the scope of this study. Possible differences should be small and with minor effect so we assume they are valid. For each station we obtain an ensemble of models from which we extract the best fitting one. We use measurements in the period range 10 s–60 s because at longer periods they are more unstable, possibly due to miscalibration of seismic stations and problems with the instrument's response. We then build maps of crustal structure in northern Italy by interpolating the values of δv_S in each layer and in each profile within the geographical boundaries of our study region. The interpolation uses ordinary kriging (Davis, 2002), a technique widely used in geophysical studies because it allows to take into account the uneven spacing among interpolated points. This leads to an updated crustal model, MAMBo-E, which has the same layered structure as MAMBo, but with laterally varying v_S (and scaled density and v_P) constrained by the ellipticity data.

4. Synthetic tests

Before proceeding to invert real data, we test the inversion procedure by attempting retrieval of synthetic, known, models for which we simulate the observations they would yield. The inversion of such simulated observations gives us key information about the benefits and drawbacks of our approach. The first such experiment is designed to evaluate the ability of the method to retrieve a realistic v_S profile, given a slightly different prior model. We choose a sample station (PRMA; Fig. 5), and take the layered structure beneath that station from model MAMBo. This will be our a priori model. To simulate a different 'real' model, we modify this v_S profile from MAMBo, by scaling its shear wave velocity gradients by a factor. We obtain a modified model with the same

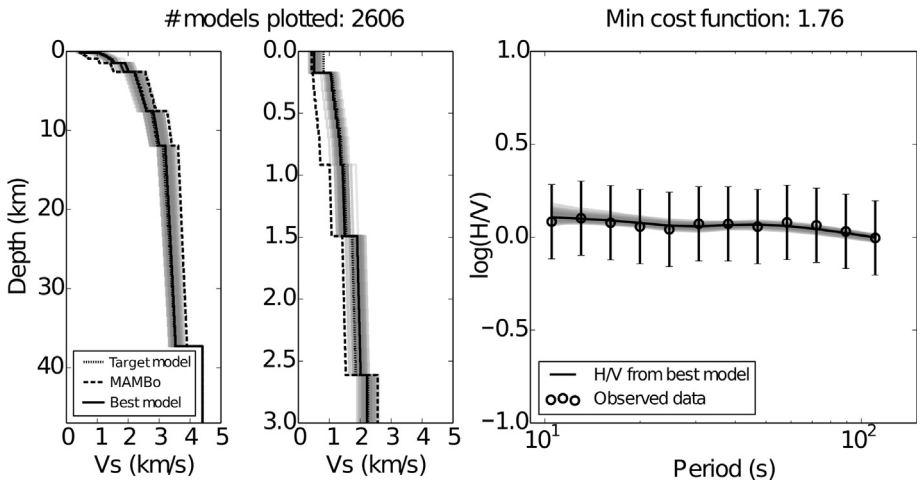

Fig. 6. Recovery test of a modified MAMBo profile (see main text). Left panel: target model used for the simulation (dotted line), model MAMBo used as a priori model (dashed line), and best-fitting model resulting from the inversion (solid line). Middle panel: magnification of the first 3 km depth. Right panel: Synthetic data (circles, with error bars) calculated for the target model using a normal mode scheme, with noise added and synthetic ellipticity curve (solid line) calculated for the best-fitting model found. The grey lines correspond to models with a cost function within 10% of the best model (left) and the associated theoretical ellipticity curves (right).

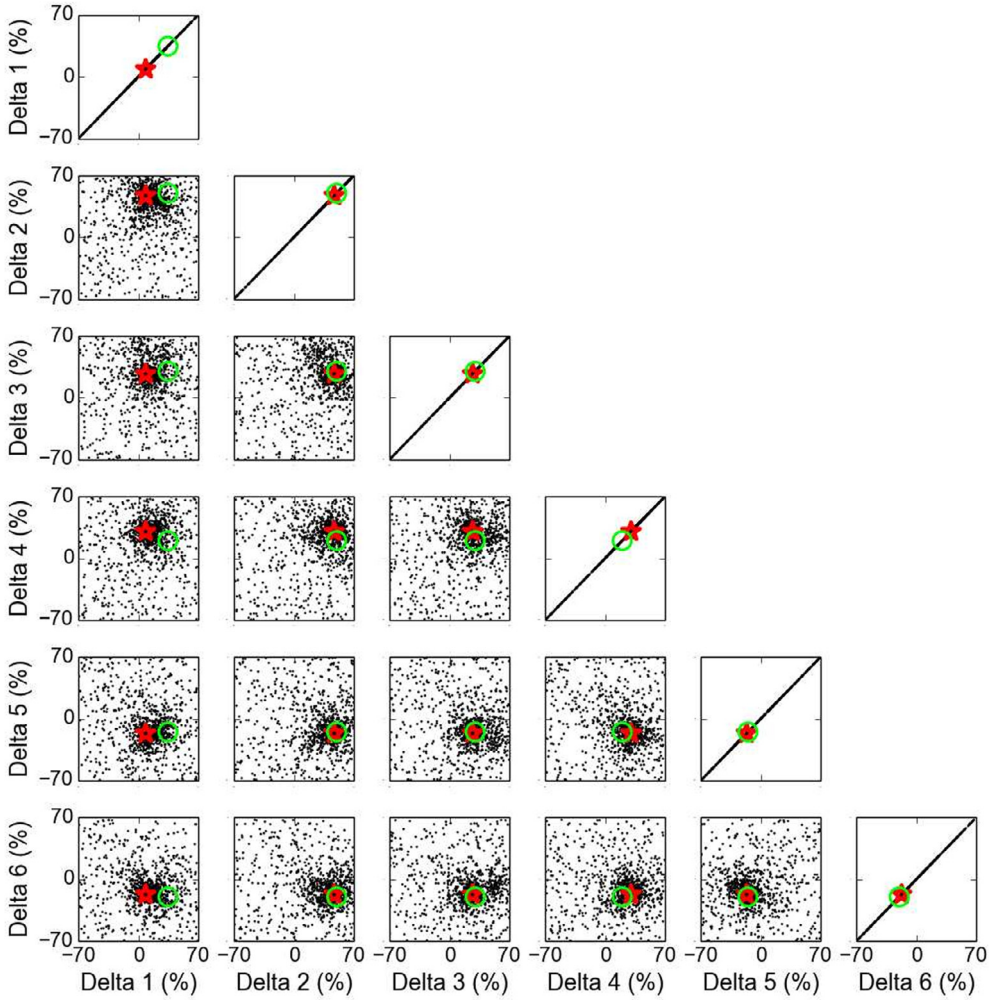

Fig. 7. Marginal model density distributions on all pairs of velocity parameters for the test in Fig. 6. Black dots: models sampled; Red star: best-fitting model found. Green circle: target model. Each point represents a model sampled during the inversion and it shows the value of the percentage anomaly from the reference model MAMBo relative to different layers (for example, Delta 1 is the percentage anomaly for layer 1). If there was a trade-off between two layers then the cloud of points will show a distribution along the diagonal. Since the clouds are denser around the best value without showing any directivity, there is no significant correlation between parameters in the various layers.

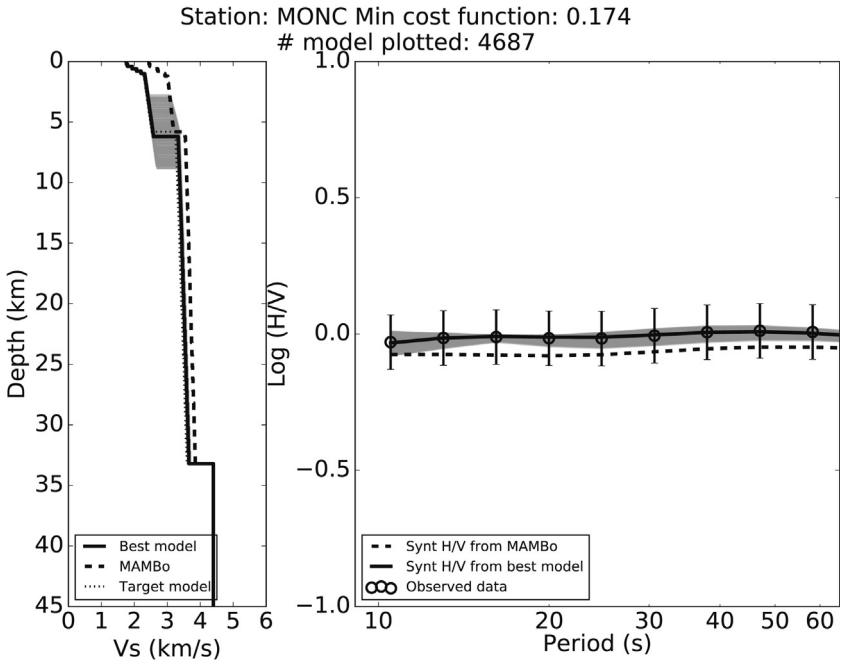

Fig. 8. Synthetic recovery test when inverting jointly for shear wave speed and thickness of a layer. Left panel: target model used for the simulation (dotted line), model MAMBo sampled beneath station MONC, which is used as a priori model (dashed line), and best-fitting model resulting from the inversion (solid line). Right panel: Synthetic data (circles, with error bars) calculated for the target model using a normal mode scheme, with noise added; theoretical H/V from model MAMBo at the sample station MONC (dashed line); and, synthetic ellipticity curve (solid line) calculated for the best-fitting model found. The grey lines correspond to models with a cost function within 10% of the best model (left) and the associated theoretical ellipticity curves (right). Note that the errors in v_S are generally smaller than $\approx 0.3\%$ and thus are not visible in the figure; the models in grey on the left have errors in layer's thickness, which lead to velocity jumps away from the discontinuity in the target model.

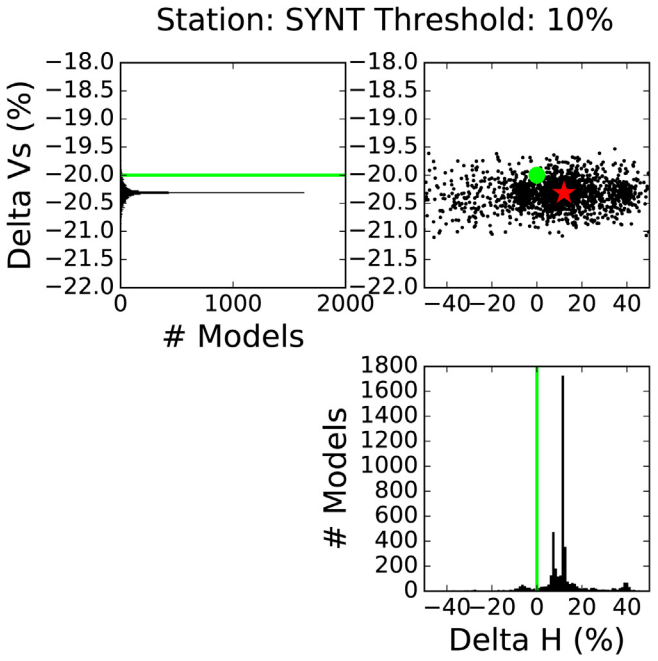

Fig. 9. Trade-off between v_S and layer thickness H (only models with cost function within 10% of minimum misfit are shown). Left: Histogram of the percentage variation of v_S in the best models sampled during the inversion. Right bottom: Histogram of the percentage variations of the thickness H during the inversion. Right top: Trade-off between the parameters and best-fitting model found (red star). The green lines/point represent the target model (δv_S measured with respect to a priori model MAMBo). (For interpretation of the references to colour in this figure legend, the reader is referred to the web version of this article.)

layered structure but different velocities in each layer, which represents our target model. We use this target model to calculate a synthetic ellipticity curve using a normal mode approach. To reproduce more realistically the observed data, we add some noise to the computed ellipticity curves: we compute 200 theoretical ellipticity curves (a number of events consistent with the real case) adding a Gaussian random noise to each point with a standard deviation 0.2 (similar to observed errors). Each curve will simulate a single event with the relative measurement error. We then take the median and percentiles as in real measurements (Berbellini et al., 2016). We use this ellipticity curve as observed data for the inversion, as described in the previous section, and invert it.

Fig. 6 shows the results of this test. The solid black line shows the best-fitting model, whereas the grey lines correspond to models with a cost function within 10% of the best model, which give empirical information about model's errors. We see that the true model is correctly retrieved, except for the first shallowest layer, where the final model stays close to the a priori one. This is due to the fact that the first layer is too thin to be uniquely resolved by our data, so the inversion procedure prefers to keep the value of this layer close to the reference a priori model. The first layer is indeed about 0.2 km thick, thinner than the vertical resolution that we infer from further resolution synthetic tests (see Supplementary Materials, Figs. S1–S6), which show that the thinnest layer that our data can resolve is 500 m thick. Fig. 7 shows the density distribution of acceptable models, projected on the subspace of all pairs of parameters. Such marginal density distributions represent a useful tool to analyse possible correlation between model parameters in retrieved models and the presence of trade-offs. Boxes along the main diagonal in fact represent (trivial) correlation of each parameter with itself, so model values are distributed along a line. Any other box shows acceptable models generally clustered around the best fitting one (red star), with no apparent correlation or directivity on the model cloud, compared with the target values (represented by green circles). These plots show that model parameter 1 (velocity in the first layer) is slightly underestimated, but this comes with no specific correlation with velocity

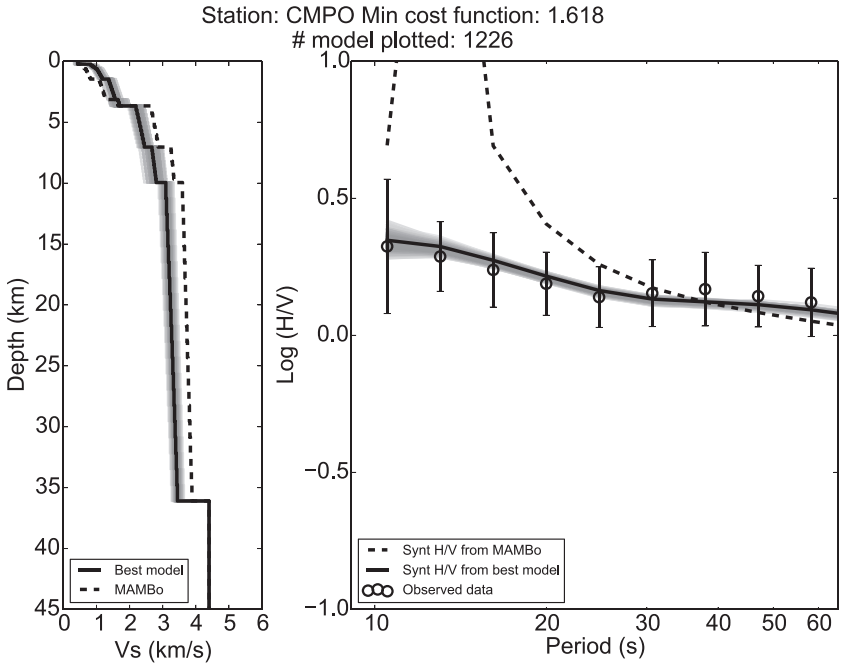

Fig. 10. Real data inversion results for shear wave velocity profile beneath station CMPO. Left: best-fitting model found (black line) compared to MAMBo (dashed line). Grey lines show models with misfit within 10% from the best model. Right: observed data (black circles with error bars) compared to H/V synthetic values from MAMBo (dashed line) and theoretical predictions of H/V from best-fitting model found (black solid line).

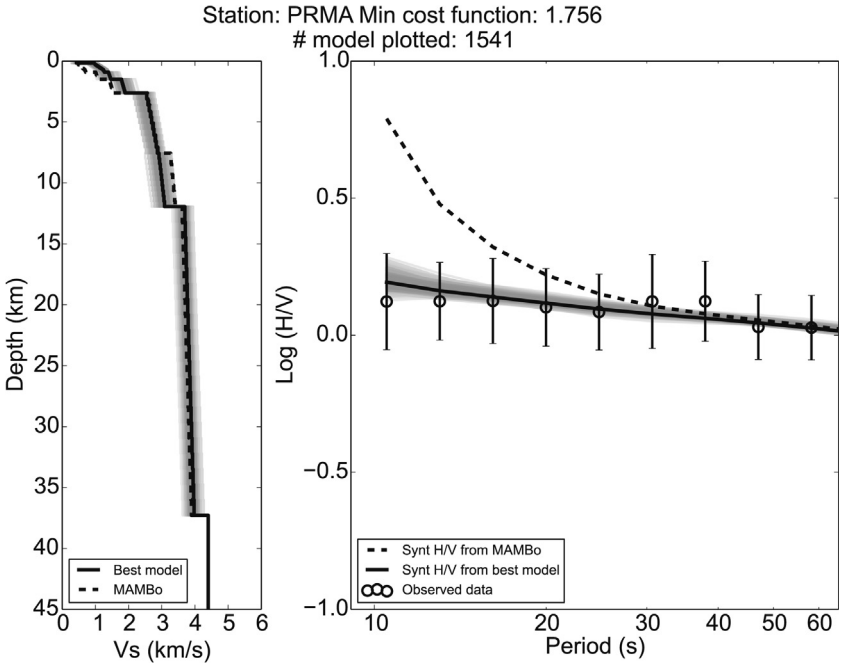

Fig. 11. Real data inversion results for v_S profile beneath station PRMA. Left: best-fitting model found (black line) compared to MAMBo (dashed line). Grey lines show models with misfit within 10% from the best model. Right: observed data (black circles with error bars) compared to H/V synthetic values from MAMBo (dashed line) and H/V synthetic values from best-fitting model found (black solid line).

in the other layers (boxes on first column). Layer 1 is very thin, and the fact that it is — even rather loosely — constrained by a slower a priori value, is the main reason for this slight under-estimation. Velocity in all the other layers is well retrieved.

We perform a further synthetic recovery test to test trade-offs between thickness and shear-wave velocity of a sedimentary layer. We set as a priori model the local velocity profile for station MONC in MAMBo (Fig. 8). We define our target model by decreasing v_S in two contiguous layers. We compute the ellipticity curve for the target model, and contaminate it with noise as in the previous synthetic test. We then invert the computed ellipticity for both layer thickness (i.e., the depth of the interface between the layers) and shear-wave velocity in the layers. The results are shown in Fig. 8. We notice that the inversion is able to correctly retrieve the v_S profile with an error of ≈0.3% (the corresponding error range is too small to be visible in the x-axis variability of the grey lines),

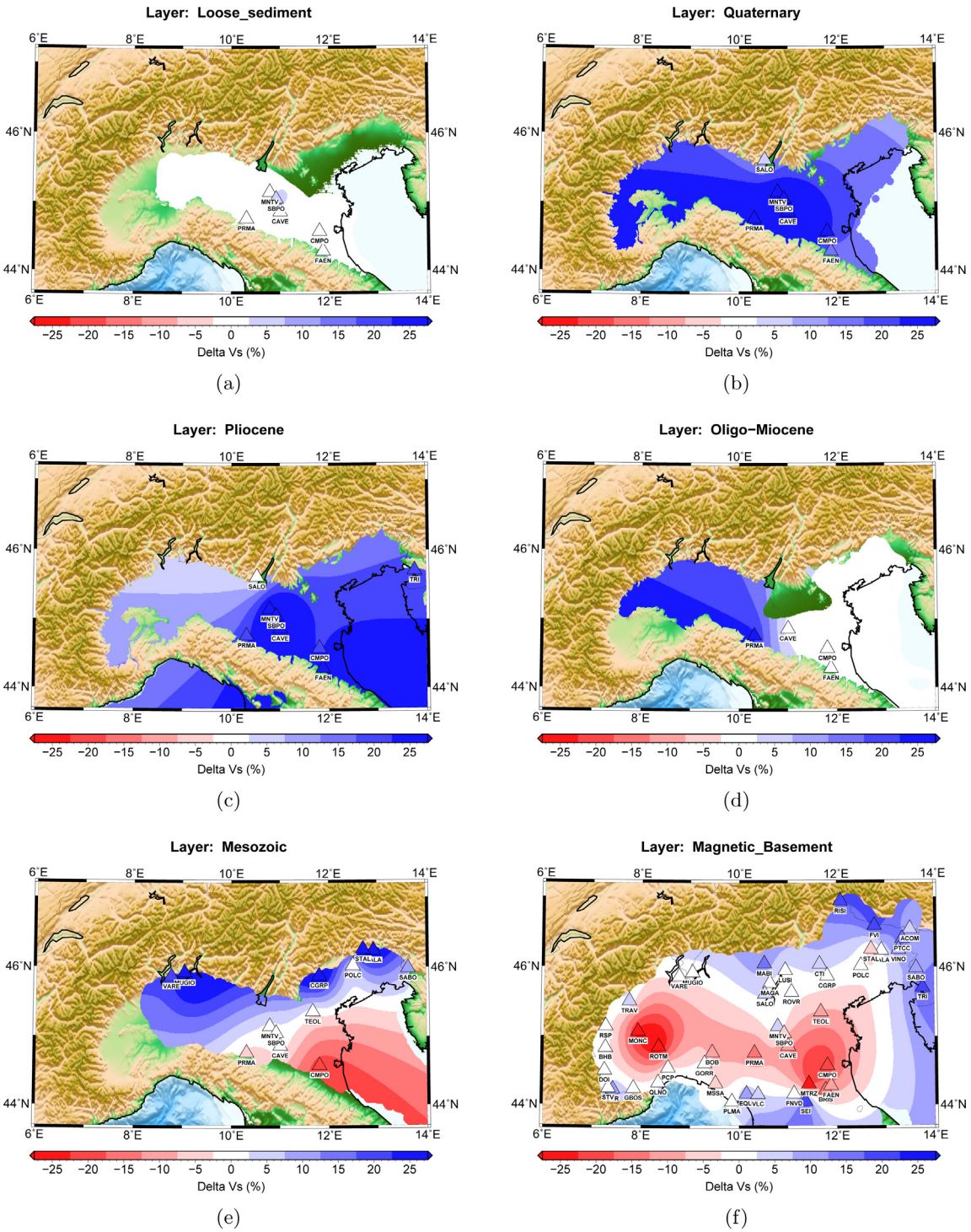

Fig. 12. Percentage shear wave velocity difference between MAMBo-E and MAMBo for the loose sediment layer (a), Quaternary layer (b), Pliocene layer (c), Oligo-Miocene layer (d), Mesozoic layer (e) and magnetic basement (f) see also Fig. 2.

whereas the layer thickness is not very well constrained: while the best fitting model matches the target layer thickness well (≈ 1 km difference), the suite of acceptable models (in grey in Fig. 8) spans a wide depth range. We also plot the correlation between the percentage variation of v_S compared to the retrieved percentage variations of the layer thickness (Fig. 9). This clearly shows that when inverting simultaneously for layer thickness and shear wave speed, the layer's thickness is constrained more poorly than v_S. Moreover, most retrieved models show thicker layers associated with lower v_S than in the target model.

Three further synthetic recovery tests are presented in the Supplementary Materials (Figs. S1–S6), showing that our approach is able to resolve 0.5 km thick layers just beneath the surface. As expected, the resolving power decreases with depth, but our tests suggests that the errors in the retrieved v_S do not exceed $\approx 8\%$ down to 20 km depth.

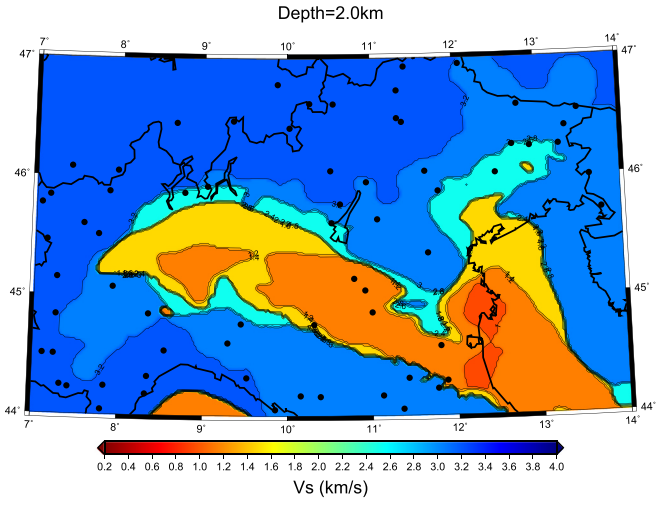

(a)

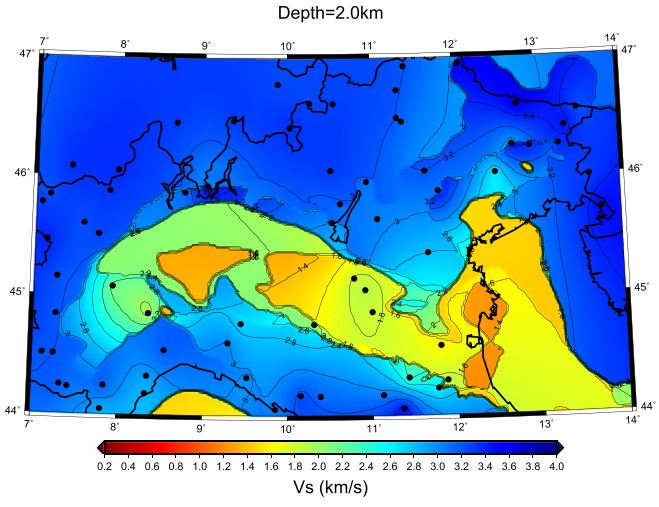

(b)

Fig. 13. Shear wave velocity at 2 km depth for MAMBo (a) and MAMBo-E (b). Stations used in the inversion are shown with black dots.

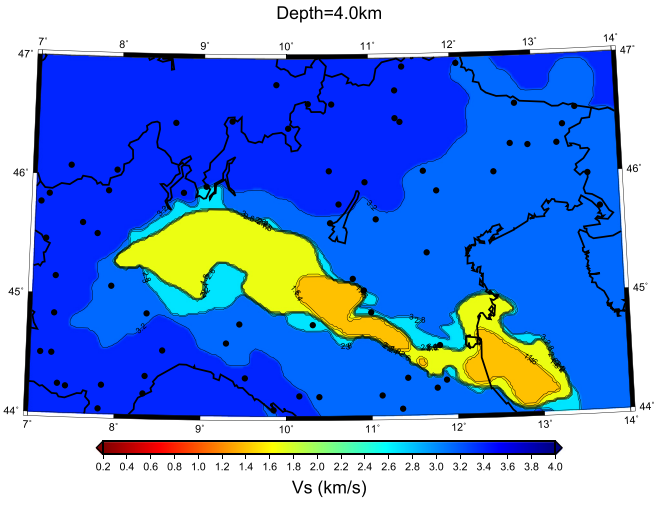

(a)

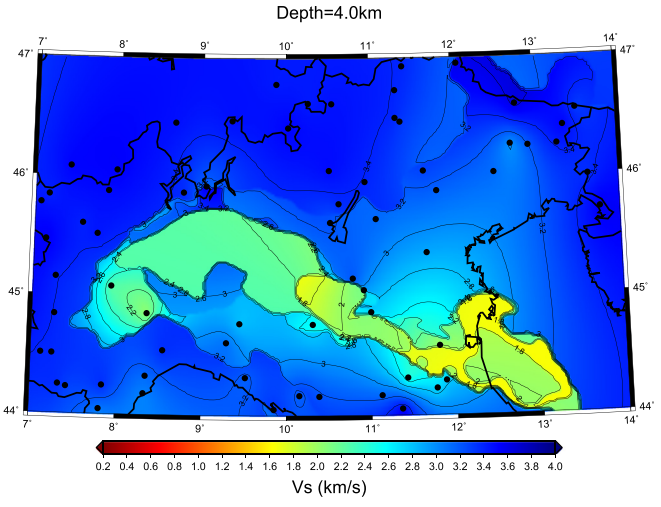

(b)

Fig. 14. Shear wave velocity at 4 km depth for MAMBo (a) and MAMBo-E (b). Stations used in the inversion are shown with black dots.

5. Results

In this section we show results from our real data ellipticity inversions using as vertical parameterisation the layered structure in the MAMBo model, which is also our a priori model. We invert for v_S, v_P and density simultaneously in each layer (v_p and density are scaled from v_S using relations by Brocher (2005)) using the approach tested through the synthetic tests presented in the previous section. We show only the results for v_S because it is the parameter with the highest sensitivity (see Fig. 3), but ellipticity showed a non-negligible sensitivity also to density. Density and shear-wave velocity are not easily separable using these data alone, so we chose to invert them together, scaling them by empirical relations. We first present detailed results for stations CMPO (Figs. 10 and S8 in Supplementary Material) and PRMA (Figs. 11 and S9 in Supplementary Material), both located in the Po Plain (see, e.g., Fig. 5). Similar to the synthetic tests, for each station we show the best fitting model found (black solid line), models with a cost function within 10% of the best-fitting model (grey lines) and the corresponding profile from the model MAMBo (dashed line). We also plot observed data (black circles with error bars) compared to the theoretical H/V curves from model MAMBo, the predicted H/V curve from the best-fitting model (black solid line) and predicted H/V curves from the models with a cost function within 10% of the best-fitting model. As we can see, for both stations the best fitting model reaches a good fit of the observed data, while the synthetic H/V curve from model MAMBo is much larger than the observed values, especially for the CMPO station.

Once we find the best-fitting models for all the stations, we interpolate v_S in each layer among the applicable stations (layers laterally thin and pinch out, so they are not always present beneath every station). This leads to a laterally varying model of v_S within each structural element (layer). The structure of the layers is shown in Fig. 12, where we — separately, and for each layer — plot the percantage variation in shear wave velocity between our new crustal model (MAMBo-E) and MAMBo (see also Fig. 2). Note that these layers vary, not only in thickness, but also in depth, so these maps are not at constant depth (constant depth maps are shown in Figs. 13–15). The loose sediments layer (Fig. 12a) does not show very large differences between MAMBo-E and MAMBo, with differences δv_S being mostly in the order of −2.5% to +2.5%. This is probably due to the very thin top layer that is not always resolved by the inversion, as we showed in the previous section. For Quaternary (Fig. 12b) and Pliocene (Fig. 12c) layers, v_S is in general

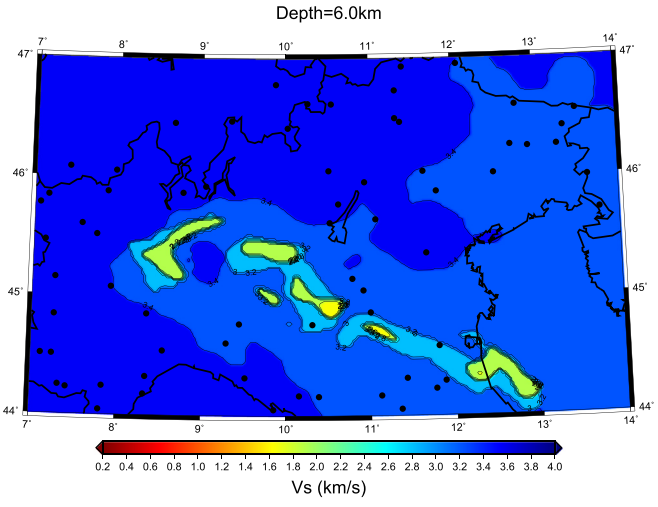

(a)

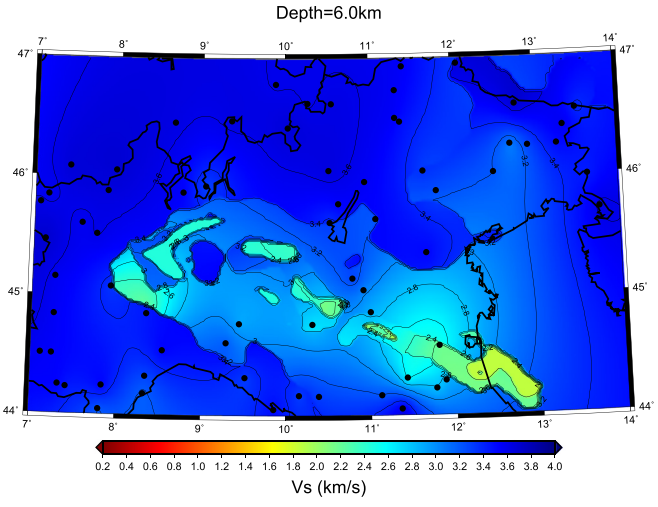

(b)

Fig. 15. Shear wave velocity at 6 km depth for MAMBo (a) and MAMBo-E (b). Stations used in the inversion are shown with black dots.

faster than in MAMBo by about 10–25%. The Oligo-Miocene layer (Fig. 12d) shows faster velocity in the western part of the Plain, while no substantial differences are seen in the eastern part. The Mesozoic layer (Fig. 12e) shows faster shear-wave velocity in the northern and western part of the Plain than in MAMBo, while lower velocities are seen in the southern-eastern part. In the middle of the Plain there are no substantial differences from MAMBo. The magnetic basement layer (Fig. 12f) shows two low velocity zones corresponding to stations MONC, ROTM (western part of the Plain) and CMPO, MTRZ (eastern part of the Plain), with intermediate velocity values between them. At the margins of the Plain the shear wave velocities are in general lower than in MAMBo.

6. Discussion

Fig. 13 shows the shear-wave velocity at a constant depth of 2 km. Model MAMBo (13a) shows considerable contrast in velocity beneath the Alps and the Apennines, as opposed to the Plain. Beneath the Alps, shear-wave velocity reaches the value of 3.2 km/s in crystalline granitic rocks. Beneath the Plain, v_S is much lower, down to 1.0 km/s in the eastern part of the Plain. Here the shallowest crust is made of the most recent (and relatively loose) sediments, carried by the Po River. The structure beneath the Apennines shows lower velocity (3.0 km/s) than in the Alps, a difference that can be linked to different lithological structure, with lower velocity of clastic sedimentary rocks. Fig. 13b shows the same v_S section for model MAMBo-E. The layered structure is the same as MAMBo, and the main features are thus inherited, but we focus on the lateral variations of shear-wave velocity within the large domains, which are laterally uniform in the top panel. We see here that the contrast between shear wave speed beneath the Plain and the mountains is smaller, with values under the Plain not lower than 1.4 km/s in the eastern part of the Plain and v_S beneath the Alps reaching 3.0 km/s. Shear-wave velocity beneath the Apennines decreases going away from the southern border of our box (that somehow follows the topographic crest) as we could expect from the different age and origin of the rocks. The southern part of the Tuscany-Ligurian Apennines is composed by Oligo-Miocene basin deposits, while the northern part is made of Jurassic-Early Cenozoic deepwater sedimentary melange and ophiolites (Thomson et al. (2010)). The Apennine region is quite tectonically active, with moderate seismicity (see Fig. 1). Shear-wave velocity beneath the Alps shows a more uniform shape, with a decrease of velocity from the north to the south-east. The Eastern Alps show quite a more complex structure, with higher velocities on the north-east and lower velocities in the south. There are not many previous studies of the seismic wave velocity at such shallow depth. For example, the inversion of the TRANSALP wide-angle seismic profile (Bleibinhaus and Gebrande, 2006), roughly along the 12°E meridian, shows relatively high P-wave velocity at about latitude 47°N and south of 47°S, which is in good qualitative agreement with our results in Fig. 13b.

The velocity structure in the Po Plain shows the most interesting features. In the western part of the Plain, in the Monferrato area, it is evident that model MAMBo-E shows lower shear-wave velocities than MAMBo ($v_S \approx 2.2$ km/s), similar to values of the Plain, while MAMBo predicted values similar to the Apennines. A similar result has been also found by Molinari et al. (2015b). This area in fact corresponds to the Monferrato sedimentary basin, characterised by Upper Eocene – Miocene shallow water clastic and carbonate facies (Mosca et al., 2010). This is different from the larger Po Plain basin, which originated mostly from Ligurian Apenninic sediments (Biella et al., 1997), but has similar seismic features. Thus, in MAMBo-E this region is assimilated to the Po Plain (this result is well-documented by two stations MONC and ROTM). On the contrary, MAMBo maps it as belonging to the Apenninic domain, because of a lack of available seismic lines in this area. While the south-western extension of the basin is not well constrained by the only two stations available in the region, MONC and ROTM, with the shear wave speed being smoothed towards the a priori values, it is nonetheless significant that this missing basin in MAMBo has been detected by ellipticity data alone.

In the central part of the Plain we notice a small area, located around coordinates $11°E - 45°N$, with slightly higher velocity (≈ 1.8 km/s) than the surrounding area (≈ 1.6 km/s). This feature is evident in the shallowest crust only, while it is not visible at 4 and 6 km depth (see Figs. 14b and 15b). This is well documented by three stations: MNTV, CAVE and SBPO. This higher velocity region may be possibly due to non-uniform composition of the shallowest sedimentary layers. However, we do not have sufficient geological information to better interpret this feature and we will comment it in more detail in the discussion of vertical cross-sections below. The easternmost part of the Plain is characterised by a small area with very low shear-wave velocities, due to the most recent and loose river deposits. This feature is inherited from the starting model MAMBo.

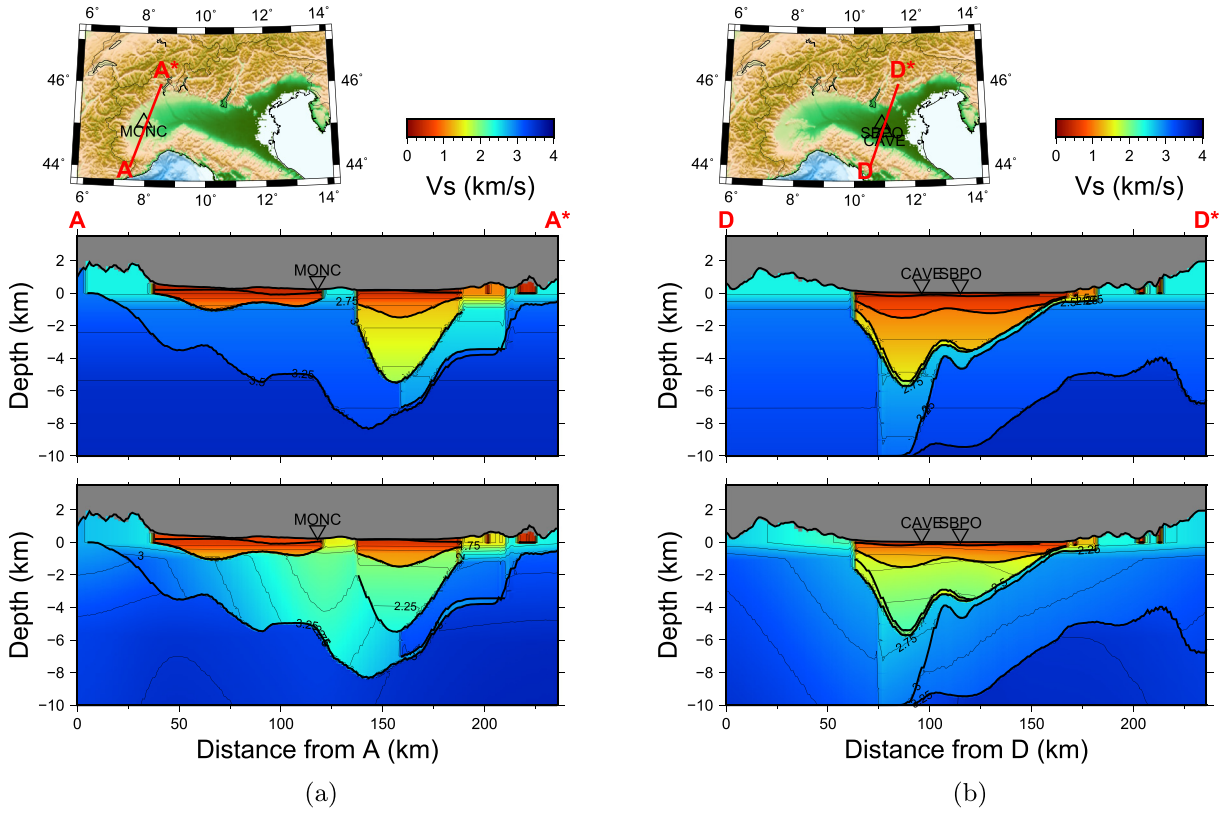

Fig. 16. Vertical cross-section of model MAMBo (top) and MAMBo-E (bottom).

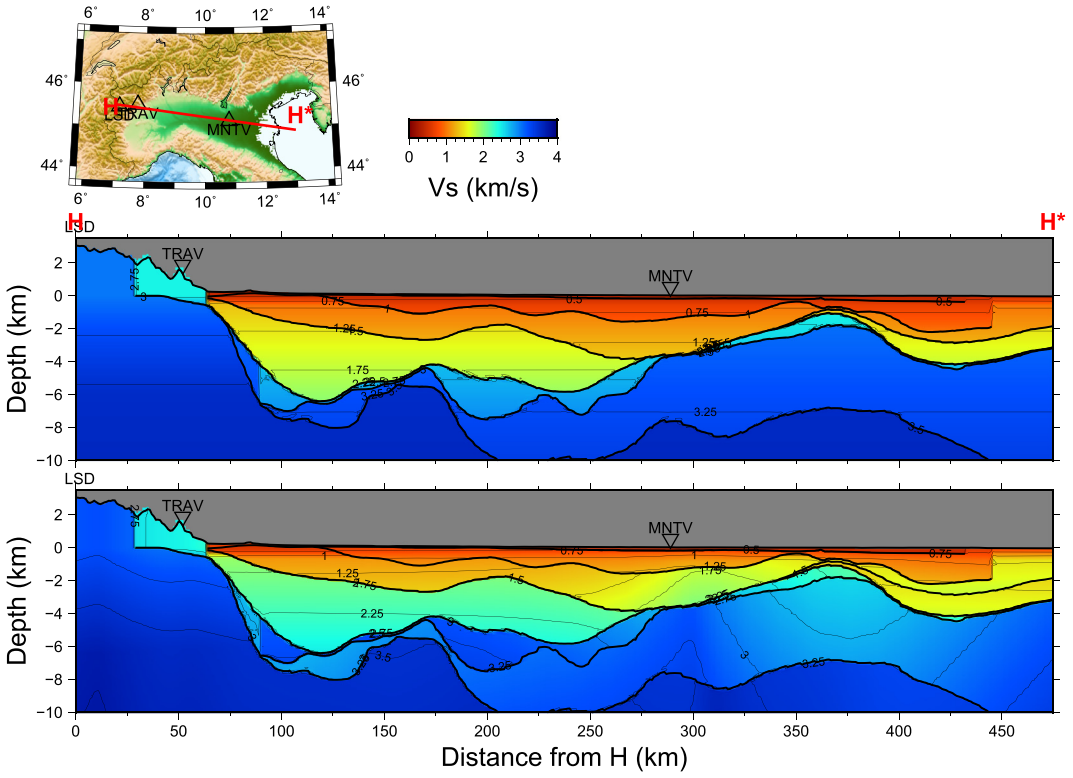

Fig. 17. Vertical cross-section of model MAMBo (top) and MAMBo-E (bottom).

The horizontal section at 4 km depth (Fig. 14) shows more uniform features than at 2 km depth, with a lower contrast between the Plain and mountains than in MAMBo. The structures beneath the Alps and the Apennines show a shape similar to those at 2 km depth, with lower velocity beneath the Apennines than the Alps. Sedimentary layers beneath the Po Plain are less extended

at this depth. Similar to the results for 2 km depth, in MAMBo-E we also observe the Monferrato basin. In the eastern part of the plain, a broad low velocity heterogeneity is located near coordinates 11.5°*E*–44.5°*N* corresponding to the thrust system located between the Ferrara-Romagna Arc and the Pedeapeninnic thrust front (FRA, PATF Fig. 1). This low velocity anomaly is well-documented by a number of recording stations, and it may be explained as a large-scale lateral variation of shear-wave velocity in the Mesozoic layer, possibly due to different composition of sedimentary rocks.

The depth section at 6 km (Fig. 15) shows an even more uniform pattern of shear-wave velocities. Here the large-scale low velocity anomaly in the eastern part of the Po Plain that we just discussed is very clear.

Vertical cross sections help gaining a better understanding of the three-dimensional variations of the model. Section A (Fig. 16a) shows a cut through the model in the western part of the Plain. We confirm that around station MONC, ≈ 120 km from point A, model MAMBo-E has lower v_S values than MAMBo, similar to the values in the Plain (this has been remarked already, and put in connection with the Monferrato basin). This low-velocity anomaly goes down to 6 km depth. The main filling of the Po Plain sedimentary basin, however, is now slightly faster than in the starting model, with a less evident discontinuity.

Vertical section D (Fig. 16b) shows the vertical structure around the central high-velocity zone that we have noticed in Fig. 13. Vertical section H (Fig. 17) presents a complete cross-section across the whole Po Plain. Here we notice both a high-velocity anomaly beneath station MNTV, at ≈ 2 km depth, and a low-velocity anomaly at around 365 km from point H, at a depth of 2–6 km. We remark again that the high-velocity bump is located near station MNTV; therefore, it is required by the data and it is not an artefact. Nevertheless, as seen in the synthetic test in Fig. 9 errors in the depth of the interface could give rise to errors in the retrieved shear wave speed (e.g., a thinner layer than in reality could lead to an artificially faster layer).

7. Conclusions

We built MAMBo-E, a new crustal seismic model of shear-wave velocity beneath the Po Plain and surrounding areas. MAMBo-E combines the detailed stratification information of MAMBo (that included data from seismic prospection and other geological data) with shear wave speed constrained by Rayleigh-wave ellipticity data. We developed a new scheme that retrieves velocity profiles from ellipticity data using a non-linear Monte Carlo inversion technique based on the Neighbourhood Algorithm by Sambridge (1999). Previous studies such as by Lin et al. (2012) showed that H/V ratios are a useful seismic parameter to better constrain the shallowest part of the crust in a joint inversion with phase-velocities measurements. Yano et al. (2009) inverted H/V ratios curves using a linearised iterative technique and demonstrated that the results have a strong dependency on the starting a priori model. We used the MAMBo model as a priori model in the inversion, and the geometry of its 3D shapes as constraints. Our study shows that fully non-linear Monte Carlo inversion of H/V ratios alone is able to constrain crustal shear wave speed, with negligible dependency on local minima set by the initial a priori model. Inversion of H/V ratios is independent from other seismic observables, such as phase or group velocities, and is performed using single station information. This is an important feature in case of poor or uneven coverage of seismic networks.

To validate the inversion technique and estimate its vertical resolution we perform a number of synthetic tests. The tests show that v_S is always well constrained, when the number and thickness of subsurface layers is known. Shallow layers with thickness as small as ≈ 0.5 km can be resolved and that resolution decreases as depth increases. We estimate that the inversion is able to resolve a layer ≈ 2 km thick at 5 km depth.

MAMBo-E shows many shallow crustal features that correlate well with the surface's geology, such as distinct faster seismic wave speed beneath the Alps and Apennines than in the Po Plain, as expected. When compared with MAMBo, MAMBo-E clearly shows a low velocity anomaly corresponding to the Monferrato sedimentary basin in the western part of the study region, which was not seen in MAMBo. Moreover, MAMBo-E seems to better delineate the Po Plain at depth, notably by suggesting that the Monferrato basin is part of the Po Plain rather than of the Apennines domain. In addition, in the Quaternary, Pliocene and Oligo-Miocene layers, MAMBo-E overall shows higher seismic wave speeds than MAMBo. Finally, a low velocity anomaly is mapped in the Mesozoic layer in the thrust system between the Ferrara-Romagna Arc and the Pedeapenninic thrust front.

Independent information on the presence and location of discontinuities and sharp gradients, both in the vertical and horizontal directions, may be necessary to drive interpolations between the various seismic stations. When this information is available, such as in our case, H/V ratios prove reliable and very valuable at imaging the shallow crustal structure. The resulting model incorporates critical information about shear-wave structure at shallow depth, which is key for accurate simulations of seismic wave propagation and hence seismic shaking in sedimentary basins. Although we expect that our modification of model MAMBo is likely to improve performance in numerical simulation of seismic wave propagation across the sedimentary basin, actual calculations are beyond the scope of this study.

Acknowledgement

Data analysis and measurements have been performed using ObsPy (Beyreuther et al., 2010; Megies et al., 2011; Krischer et al., 2015). Plots and maps in this paper have been made using Generic Mapping Tools by Wessel et al. (2013). AMGF thanks funding by the Fundação para a Ciência e Tecnologia (FCT) project AQUAREL (PTDC/CTE-GIX/116819/2010) and computing time in the UK supercomputer Archer. AMGF is also grateful for funding from NERC project NE/K005669/1. We acknowledge discussions and mobility supported by COST Action ES1401-TIDES.

Appendix A. Supplementary data

Supplementary data associated with this article can be found, in the online version, at http://dx.doi.org/10.1016/j.pepi.2016.12.005.

References

Aagaard, B.T., Brocher, T.M., Dolenc, D., Dreger, D., Graves, R.W., Harmsen, S., Hartzell, S., Larsen, S., McCandless, K., Nilsson, S., Petersson, N.A., Rogers, A., Sjorreen, B., Zoback, M.L., 2008. Ground-motion modeling of the 1906 San Francisco Earthquake, Part II: ground-motion estimates for the 1906 earthquake and scenario events. Bull. Seism. Soc. Am. 98, 1012–1046.

Bard, P.Y., Campillo, M., Sānchez-Sesma, F., Chāvez Garcia, F.J., 1998. The mexico earthquake of september 19, 1985-a theoretical investigation of large-and small scale amplification effects in the mexico city valley. Earthquake Spectra 4 (6), 609–633.

Barrier, E., Chamot-Rooke, N., Giordano, G., Morelli, A., Brouillet, J.-F., 2005. An innovative cartographic concept – The Geodynamic Map of the Mediterranean. EPISODES 28 (3), 193–196.

Berbellini, A., Morelli, A., Ferreira, A.M.G., 2016. Ellipticity of Rayleigh waves in basin and hard-rock sites in Northern Italy. Geophys. J. Int. 206 (1), 395–407. http://dx.doi.org/10.1093/gji/ggw159.

Beyreuther, M., Barsch, R., Krischer, L., Megies, T., Behr, Y., Wassermann, J., 2010. ObsPy: A Python Toolbox for Seismology. SRL 81 (3), 530–533. http://dx.doi.org/10.1785/gssrl.81.3.530.

Biella, G., Polino, R., Franco, R.D., Rossi, P.M., Clari, P., Corsi, A., Gelati, R., 1997. The crustal structure of the western Po plain: reconstruction from integrated geological and seismic data. Terra Nova 9, 28–31. http://dx.doi.org/10.1046/j.1365-3121.1997.d01-5.x.

Bleibinhaus, F., Gebrande, H., 2006. Crustal structure of the Eastern Alps along the TRANSALP profile from wide-angle seismic tomography. Tectonophysics 414, 51–69. http://dx.doi.org/10.2016/j.tecto.2005.10028.

Bradley, B.A., 2012. Strong ground motion characteristics observed in the 4 September Darfield, New Zealand earthquake. Soil Dyn. Earthquake Eng. 42, 32–46.

Brocher, T.M., 2005. Empirical relations between elastic wavespeeds and density in the Earth's crust. Bull. Seism. Soc. Am. 95, 2081–2092.

Chaljub, E., Moczo, P., Tsuno, S., Bard, P.-Y., Kristek, J., Käaser, M., Stupazzini, M., Kristekova, M., 2010. Quantitative comparison of four numerical predictions of 3D ground motion in the Grenoble valley, France. Bull. Seism. Soc. Am. 100, 1427–1455.

Davis, J., 2002. Statistics and Data Analysis in Geology. John Wiley & Sons.

Dhakal, Y.D., Yamanaka, H., 2013. An evaluation of 3D velocity models of the Kanto basin for long-period ground motion simulations. J. Seismol. 17, 1073–1102.

Diehl, T., Husen, S., Kissling, E., Deichmann, N., 2009. High-resolution 3-D P-wave model of the alpine crust. Geophys. J. Int. 179 (2), 1133–1147.

Dujardin, A., Causse, M., Courboulex, F., Traversa, P., 2016. Simulation of the basin effects in the Po Plain during the Emilia-Romagna seismic sequence (2012) using empirical Green's functions. Pure Appl. Geophys. http://dx.doi.org/10.1007/s00024-015-1233-4.

Dziewonski, Adam M., Anderson, Don L., 1981. Preliminary reference Earth model. Phys. Earth Planet. Interiors 25 (4), 297–356. http://dx.doi.org/10.1016/0031-9201(81)90046-7.

Ferreira, A.M.G., Woodhouse, J.H., 2007a. Source, path and receiver effects on seismic surface waves. Geophys. J. Int. 168, 109–132.

Ferreira, A.M.G., Woodhouse, J.H., 2007b. Observations of long period Rayleigh wave ellipticity. Geophys. J. Int. 169, 161–169.

Gualtieri, L., Serretti, P., Morelli, A., 2014. Finite-difference P-wave travel time seismic tomography of the crust and uppermost mantle in the Italian region. Geochem. Geophys. Geosyst. 15, 69–88. http://dx.doi.org/10.1002/2013GC004988.

Herrmann, R.B., 2013. Computer programs in seismology: an evolving tool for instruction and research. Seismol. Res. Lett. 84 (6), 1081–1088.

Koketsu, K., Kikuchi, M., 2000. Propagation of seismic ground motion in the Kanto basin. Science 228, 1237–1239.

Krischer, L., Megies, T., Barsch, R., Beyreuther, M., Lecocq, T., Caudron, C., Wassermann, J., 2015. ObsPy: a bridge for seismology into the scientific Python ecosystem. Comput. Sci. Discovery 8 (1), 014003. http://dx.doi.org/10.1088/1749-4699/8/1/014003.

Lin, F.-C., Schmandt, B., Tsai, V.C., 2012. Joint inversion of Rayleigh wave phase velocity and ellipticity using USArray: constraining velocity and density structure in the upper crust. Geophys. Res. Lett. 39, L12303. http://dx.doi.org/10.1029/2012GL052196.

Megies, T., Beyreuther, M., Barsch, R., Krischer, L., Wassermann, J., 2011. ObsPy – What can it do for data centers and observatories? Ann. Geophys. 54 (1), 47–58. http://dx.doi.org/10.4401/ag-4838.

Molinari, I., Morelli, A., 2011. EPcrust: a reference crustal model for the european plate. Geophys. J. Int. 185, 352–364.

Molinari, I., Argnani, A., Morelli, A., Basini, P., 2015a. Development and testing of a 3D seismic 2 velocity model of the Po Plain sedimentary basin, Italy. Bull. Seismol. Soc. Am. 105 (2a). http://dx.doi.org/10.1785/0120140204.

Molinari, I., Verbeke, J., Boschi, L., Kissling, E., Morelli, A., 2015b. Italian and Alpine three-dimensional crustal structure imaged by ambient-noise surface-wave dispersion. Geochem. Geophys. Geosyst. 16, 2015G. http://dx.doi.org/10.1002/C006176.

Mosca, P., Polino, R., Rogledi, S., Rossi, M., 2010. New data for the kinematic interpretation if the Alps-Apennines junction (Northwestern Italy). Int. J. Earth Sci.(Geol. Rundsch.)99,833–849. http://dx.doi.org/10.1007/s00531-009-0428-2.

Nakamura, Y., 1989. A method for dynamic characteristics estimation of subsurface using microtremor on the ground surface. Q. Rep. Railway Tech. Res. Inst. 30 (1), 25–30.

Sambridge, M., 1999. Geophysical inversion with a neighbourhood algorithm – searching a parameter space. Geophys. J. Int. 138, 479–494.

Serpelloni, E., Vannucci, G., Pondrelli, S., Argnani, A., Casula, G., Anzidei, M., Baldi, P., Gasperini, P., 2007. Kinematics of the Western Africa-Eurasia plate boundary from focal mechanisms and GPS data. Geophys. J. Int. 169, 1180–1200. http://dx.doi.org/10.1111/j.1365-246X.2007.03367.x.

Stupazzini, M., Paolucci, R., Igel, H., 2009. Near-fault earthquake ground-motion simulation in the Grenoble valley by a high-performance spectral element code. Bull. Seism. Soc. Am. 99, 286–301.

Tanimoto, T., Rivera, L., 2008. The ZH ratio method for long-period seismic data: sensitivity kernels and observational techniques. Geophys. J. Int 172, 187–198.

Tanimoto, T., Yano, T., Hakamata, T., 2013. An approach to improve Rayleigh-wave ellipticity estimates from seismic noise: application to the Los Angeles Basin. Geophys. J. Int 193, 407–420. http://dx.doi.org/10.1093/gji/ggs123.

Thomson, S.N., Brandon, M.T., Reiners, P.W., Zattin, M., Isaacson, P.J., Balestrieri, M. L., 2010. Thermochronologic evidence for orogen-parallel variability in wedge kinematics during extending convergent orogenesis of the northern Apennines, Italy. GSA Bull. 122, 160–1179. http://dx.doi.org/10.1130/B26573.1.

Vannoli, P., Burrato, P., Valensise, G., 2015. The Seismotectonics of the Po Plain (Northern Italy): Tectonic Diversity in a Blind Faulting Domain. Pure Appl. Geophys. 172, 1105–1142. http://dx.doi.org/10.1007/s00024-014-0873-0.

Verbeke, J., Boschi, L., Stehly, L., Kissling, E., Michelini, A., 2012. High-resolution Rayleigh-wave velocity maps of central Europe from a dense ambient noise dataset. Geophys. J. Int. 188 (3), 1173–1187.

Wagner, M., Kissling, E., Husen, S., 2012. Combining controlled-source seismology and local earthquake tomography to derive a 3-D crustal model of the western Alpine region. Geophys. J. Int. 191 (2), 789–802.

Wessel, P., Smith, W.H.F., Scharroo, R., Luis, J., Wobbe, F., 2013. Generic mapping tools: improved version released. EOS Trans. AGU 94 (45), 409–410. http://dx.doi.org/10.1002/2013EO450001.

Yano, T., Tanimoto, T., Rivera, L., 2009. The ZH ratio method for long-period seismic data: inversion for S-wave velocity structure. Geophys. J. Int. 179, 413–424.